Nanoscale

PAPER

View Article Online
View Journal | View Issue

Cite this: *Nanoscale*, 2017, **9**, 9049

Hydrothermal and biomineralization synthesis of a dual-modal nanoprobe for targeted near-infrared persistent luminescence and magnetic resonance imaging†

Yu Wang,[a] Cheng-Xiong Yang*[a] and Xiu-Ping Yan *[a,b]

Received 22nd March 2017,
Accepted 28th May 2017

DOI: 10.1039/c7nr02038d

rsc.li/nanoscale

The development of the multimodal probes is of great importance for bioimaging application. Herein, we report the fabrication of a functional nanocomposite from near-infrared (NIR) persistent luminescent nanoparticles (PLNPs) and Gd_2O_3 as a multimodal probe for *in vivo* NIR persistent luminescence and magnetic resonance (MR) imaging. Small-sized monodispersed NIR $ZnGa_2O_4:Cr^{3+}$ PLNPs (*ca.* 15 nm) were prepared as the NIR persistent luminescence source by a hydrothermal method while hyaluronic acid (HA) functionalized Gd_2O_3 (HA-Gd_2O_3) was synthesized as the MR contrast agent *via* a biomineralization approach. An EDC/NHS coupling strategy was used to connect the amino functionalized PLNPs and the HA-Gd_2O_3 to give the HA functionalized multimodal probe. The multimodal probe not only exhibits an excellent NIR persistent luminescence signal, but also exhibits larger longitudinal relaxivity (7.38 mM^{-1} s^{-1}) than commercial contrast agent Gd-DTPA. Moreover, the HA moieties not only enhance the biocompatibility of the multimodal probe, but also endow the probe with tumor-targeting capability. Both *in vitro* and *in vivo* bioimaging experiments demonstrate the potential of the multimodal probe for tumor-targeting NIR persistent luminescence and MR imaging.

1. Introduction

Molecular imaging technologies, such as magnetic resonance imaging (MRI), computed tomography (CT) and optical imaging, are powerful tools for basic biological research, disease diagnosis and treatment.[1,2] Nevertheless, each imaging modality has its own advantages and limitations. For example, optical imaging shows high sensitivity and activatable ability, but has intrinsic limitation of poor spatial resolution. In contrast, MRI has high spatial resolution and good tissue penetration, but its application is limited by low sensitivity and high cost. Multimodal imaging technology can provide much more accurate, reliable and thorough information than the single imaging technology. So, great attention has been paid to the development of multi-modal imaging probes with at least two imaging abilities to overcome the limitations of each individual imaging technology.[3–5]

Persistent luminescent nanoparticles (PLNPs) can still emit persistent luminescence (PL) for hours or days after stopping excitation, and allow luminescence detection without the need for *in situ* excitation.[6–10] Since Scherman and co-workers introduced $Ca_{0.2}Zn_{0.9}Mg_{0.9}Si_2O_6:Eu^{2+},Mn^{2+},Dy^{2+}$ PLNPs to *in vivo* imaging,[11] there has been great interest in the application of PLNPs for biomedical research due to no autofluorescence of tissue, high sensitivity and a super signal to noise ratio (SNR).[8] $CaMgSi_2O_6:Eu^{2+},Mn^{2+},Pr^{3+}$, $LiGa_5O_8:Cr^{3+}$ and a series of Cr^{3+} doped zinc gallogermanates have been employed for bioimaging,[12–23] biosensing,[24–28] drug delivery[29–33] and tumor therapy.[34–36] Cr-doped zinc gallogermanates are more suitable for bioimaging due to superlong near-infrared (NIR) PL and rechargeable ability with red LED light. Various synthetic methods have been developed to control the size and shape of the PLNPs for better bioimaging capability.[19–23,37]

Despite these improved features of PLNPs, low spatial resolution is still the limitation of PLNPs for bioimaging. For this reason, integration of CT and magnetic resonance (MR) signals into PLNPs has been reported.[15,32,33,38,39] Abdukayum *et al.* coupled Gd-DTPA to the PLNPs to compose a MR/PL dual-modal probe.[15] Maldiney *et al.* introduced the MR signal to the PLNPs by co-doping gadolinium in the synthetic process

[a]*College of Chemistry, Research Center for Analytical Sciences, State Key Laboratory of Medicinal Chemical Biology, Tianjin Key Laboratory of Molecular Recognition and Biosensing, Nankai University, Tianjin 300071, China.*
E-mail: cxyang@nankai.edu.cn, xpyan@nankai.edu.cn; Fax: +(86)22-23506075; Tel: +(86)22-23506075
[b]*Collaborative Innovation Center of Chemical Science and Engineering (Tianjin), Tianjin 300071, China*

† Electronic supplementary information (ESI) available: Experimental details and additional figures. See DOI: 10.1039/c7nr02038d

of PLNPs.[38] Teston *et al.* embedded the ultrasmall superparamagnetic iron oxides into the mesoporous silica shell of PLNPs to fabricate the MR/PL multi-modal probe.[39] Shi *et al.*[32] and Dai *et al.*[33] prepared Gd_2O_3@mSiO_2@PLNPs with the Gd_2O_3 core acting as the MR contrast agent. Lu *et al.* fabricated core–shell structured PLNPs@TaO_x@SiO_2 with the TaO_x shell as the CT contrast agent for PL and CT imaging.[16] Even so, a simple and convenient method for the synthesis of PLNP based multimodal probes with tumor-targeting capability is still rare.

Herein, we report the design and fabrication of functional PLNP based multimodal imaging nanoprobes for targeted PL/MR dual-modal bioimaging. Hyaluronic acid (HA) functionalized Gd_2O_3 (HA-Gd_2O_3) was prepared *via* a biomineralization approach as the MR contrast agent. The NIR emitting PLNPs were synthesized by a hydrothermal method and conjugated to the HA-Gd_2O_3 to give the functional PLNP based multimodal imaging nanoprobe HA-Gd_2O_3-PLNPs. The HA moieties, which specifically target cluster determinant 44 receptors (CD44R) overexpressed in tumor cells, enable the enhancement of the biocompatibility of the multimodal probe with tumor-targeting capability. The prepared functional nanoprobe shows potential for MR/PL multimodal imaging.

2. Experimental

2.1 Preparation and functionalization of PLNPs

The PLNPs were synthesized by a hydrothermal method. Aqueous solutions of $Zn(NO_3)_2$ (5 mL, 0.2 M), $Ga(NO_3)_3$ (10 mL, 0.2 M) and $Cr(NO_3)_3$ (100 μL, 0.01 M) were mixed under vigorous stirring. The mixed solution was adjusted to pH 8 with ammonia solution, made up to 20 mL with ultrapure water, and stirred for 3 h at room temperature. The solution was then transferred to a 30 mL Teflon-lined stainless steel autoclave and reacted at 220 °C for 72 h. The resulting PLNPs were purified by centrifugation and washed three times with water and ethanol, respectively. The amino-modified PLNPs (PLNPs-NH_2) were obtained as in a previous report.[13]

2.2 Preparation of HA-Gd_2O_3-PLNPs

The HA-Gd_2O_3 was synthesized according to Wang *et al.* with some modifications.[40] Briefly, HA (200 mg) was dissolved in ultrapure water (9 mL) and $Gd(NO_3)_3$ solution (1 mL, 50 mM) was added with a 5 min stirring. The mixed solution was adjusted to pH 8 with NaOH (1 M) and reacted for 1 h with continuous stirring at room temperature. The purified product HA-Gd_2O_3 was obtained after dialysis and freeze-drying of the reactant solution.

The multimodal probe HA-Gd_2O_3-PLNPs were synthesized by amidation reaction. To avoid the formation of large aggregations, the amounts of HA-Gd_2O_3, PLNPs-NH_2 and the coupling agents were controlled. Briefly, HA-Gd_2O_3 (200 mg) was dissolved in 20 mL of PBS (20 mM, pH 6.0), to which *N*-(3-dimethylaminopropyl)-*N*′-ethylcarbodiimide hydrochloride (EDC) (4 mg) and *N*-hydroxysuccinimide (NHS) (10 mg) were added. After stirring of the above mixture solution for 2 h, 20 mL of the suspension containing PLNPs-NH_2 (40 mg) was slowly added with quick stirring and the pH was adjusted to 8 with NaOH solution (1 M). The suspension was stirred for another 24 h. The resulting HA-Gd_2O_3-PLNPs were collected after centrifugation, washed with ultrapure water and vacuum dried at room temperature.

2.3 *In vitro* cytotoxicity assay

The cytotoxicity of the HA-Gd_2O_3-PLNPs was tested by the MTT assay using HepG 2 cells and MCF-7 cells with a similar procedure as described in a previous publication.[35]

2.4 *In vitro* imaging and block experiments

HepG 2 cells (high expression of CD44R) and MCF-7 cells (low expression of CD44R) were cultured in DMEM medium with 10% FBS and 1% penicillin–streptomycin under an atmosphere containing 5% CO_2 at 37 °C. The CD44R was blocked by pre-treated HepG 2 cells with HA for 8 h. The DMEM medium containing HA-Gd_2O_3-PLNPs (50 μg mL^{-1}) was added to each well after 8 h incubation. The cells were incubated for another 4 h and washed with PBS to remove the excess probe.

2.5 *In vivo* PL imaging of HepG 2 tumor

All animal experiments were done based on the instructions of the Tianjin Committee of Use and Care of Laboratory Animals. The Balb/c nude mice (5 weeks, female) were purchased from HFK Bioscience Co. Ltd (Beijing, China). HepG 2 cells (5×10^6 cells per mouse) were subcutaneously injected into the nude mice. After the tumor had grown to 5 mm in size, the subcutaneous HepG 2 tumor-bearing mice were obtained.

The solution of HA-Gd_2O_3-PLNPs (200 μL, 1 mg mL^{-1}) was excited with 254 nm UV light for 10 min, and then injected into the HepG 2 tumor-bearing mice *via* tail vein and the luminescence images were recorded. One hour after injection, the luminescence images were acquired after a 650 nm LED light (5000 lm) irradiation on the mice for 2 min. The exposure time was 300 s.

2.6 *In vitro* and *in vivo* MR images

The MR images and relaxation time were obtained on a HT/MRSI60-60KY 1.2T MRI system (Huantong Co. Ltd, Shanghai, China). A series of aqueous solutions of HA-Gd_2O_3-PLNPs were prepared with different Gd concentrations to obtain the relaxivity (r_1).

The solution of HA-Gd_2O_3-PLNPs (200 μL, 2 mg mL^{-1}) was intravenously injected into the Balb/c nude mice with HepG 2 tumor (5 weeks, female). MR images were obtained before and at 6 h after injection.

2.7 Histological staining

The histological changes of the major organs were studied 15 days after intravenous injection of the nude mice. The mice were sacrificed and the major organs were fixed in a 4% formaldehyde solution. Finally, the standard H&E staining was carried out for histological examination.

3. Results and discussion

Scheme 1 shows the route for the preparation of HA-Gd_2O_3-PLNPs. The PLNPs were synthesized by a one-pot hydrothermal method and the surface was modified *via* the hydrolysis of (3-aminopropyl)triethoxysilane (APTES) to introduce the amino group to give PLNPs-NH_2. The HA-Gd_2O_3 probe was prepared by a biomineralization process.[40] Here, the HA moieties enable the probe to target the CD44R on the tumor cell surface. An EDC/NHS coupling strategy was employed to conjugate the amino groups of the PLNPs to the carboxyl group of HA-Gd_2O_3 to obtain the multimodal probe HA-Gd_2O_3-PLNPs.

The influence of the reaction temperature, Cr doping ratio, reaction time and reactant concentration on the luminescence intensity and afterglow time of the PLNPs was studied. The PL delay curves show that the higher reaction temperature of the hydrothermal method led to better luminescence intensity (Fig. 1A). The increase in temperature led to a sharper characteristic peak of the XRD pattern (Fig. S1A, ESI†) and a larger particle size of PLNPs (Fig. S2, ESI†). The results show that the increase in temperature favors the enhancement of crystallinity and luminescence intensity.

The delay curves of the PLNPs varied with the doping content of Cr (Fig. 1B). The PL intensity decreased with the increase of Cr content, mainly because the increased Cr emitter in the zinc gallate host led to faster release of the storage energy.[41,42] The TEM images (Fig. S3, ESI†) and XRD patterns (Fig. S1B, ESI†) show that doping Cr has no obvious influence on the particle size and crystal structure. No remarkable shift of the characteristic peak was observed with the increasing concentration of Cr. The emission spectra show that the luminescence intensity at 695 nm increased with the Cr content (Fig. S4, ESI†).

The PL intensity increased with the reaction time from 12 h to 72 h, but showed no obvious change with further increase of the reaction time to 96 h (Fig. 1C). The PL intensity also increased with the reactant concentration (Fig. 1D). TEM images show no distinct change in the particle size with the reaction time and reactant concentration (Fig. S5 and S6, ESI†). The XRD patterns indicate that the better crystallinity is responsible for the increased PL intensity (Fig. S1C and D, ESI†).

The XRD pattern shows that the synthesized PLNPs have a spinel phase of zinc gallate (JCPDS no. 38-1024) and no other characteristic peaks such as ZnO and Ga_2O_3 were observed (Fig. 2A). The HRTEM image indicates that the distance of lattice fringes is 4.82 Å, corresponding to the (111) lattice planes of the zinc gallate solid solution and the lattice defects were also observed (Fig. 2D). The HRTEM image also reveals that the prepared HA-Gd_2O_3 has a round-like shape with a size of 2.2 ± 0.3 nm (Fig. S7A and B, ESI†). The TEM image shows that the synthesized PLNPs have good dispersity and uniform shape with a size of 14.3 ± 3.2 nm (Fig. 2B and C). DLS measurements show that the hydrodynamic size of the PLNPs and HA-Gd_2O_3-PLNPs in aqueous solution is 43.8 and 141.8 nm, respectively (Fig. S8A, ESI†). No obvious change in the size dis-

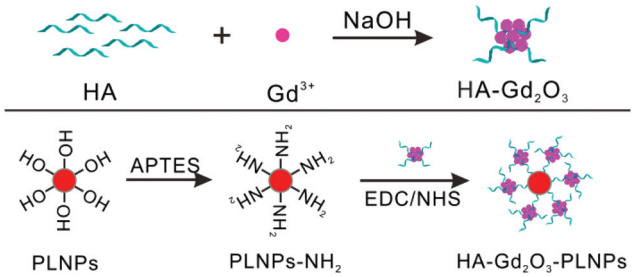

Scheme 1 Schematic for the preparation of HA-Gd_2O_3-PLNPs.

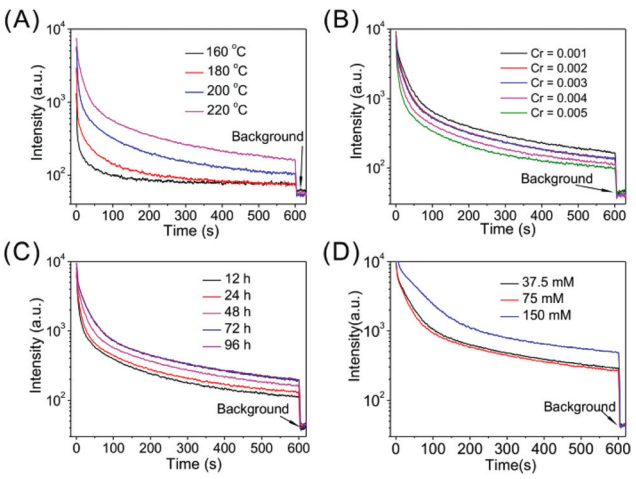

Fig. 1 NIR PL decay curves of the PLNP powder after 254 nm UV lamp excitation for 5 min: (A) $ZnGa_2O_4$:$Cr_{0.001}$ synthesized at different reaction temperatures for 24 h with 150 mM reactant concentration. (B) $ZnGa_{2-x}O_4$:Cr_x synthesized with various doping contents of Cr for 24 h with 150 mM reactant concentration at 220 °C. (C) $ZnGa_2O_4$:$Cr_{0.001}$ synthesized for different reaction times with 150 mM reactant concentration at 220 °C. (D) $ZnGa_2O_4$:$Cr_{0.001}$ synthesized with different reactant concentrations for 72 h at 220 °C.

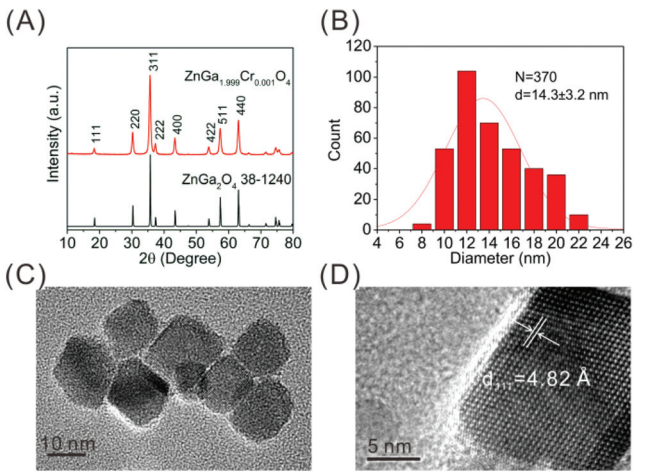

Fig. 2 (A) XRD pattern of the PLNPs; (B) size distribution of the PLNPs; (C) TEM and (D) HRTEM images of the PLNPs.

tribution in cell culture solution for 24 h shows the good stability and dispersibility of the HA-Gd_2O_3-PLNPs (Fig. S8B, ESI†). The zeta potential of the PLNPs changed from −31.6 mV to 24.2 mV after the APTES modification due to the introduced amino group, while that of HA-Gd_2O_3-PLNPs was −9.58 mV as HA is abundant in the carboxyl group (Fig. S9, ESI†).

FT-IR spectra and TGA were used to further confirm the successful modification of PLNPs. Strong absorption peaks of O–Si–O at 1120 and 1040 cm^{-1}, the asymmetric and symmetric CH_2 stretching bands at 2929 and 2872 cm^{-1}, and the N–H stretching bands at 3415 and 3284 cm^{-1} indicate the successful amino-functionalization of PLNPs.[13] The strong absorption bands of –COO at 1620 and 1076 cm^{-1} in HA-Gd_2O_3-PLNPs suggest successful conjugation of HA-Gd_2O_3 to the PLNPs. Two absorption bands of CO-NH were overlapped with the absorption band of –COO at 1620 cm^{-1} (Fig. 3A).[43] The TGA curves of PLNPs-NH_2 show a weight loss for the evaporation of the absorbed water below 125 °C and the decomposition of the alkane on the particle surface after 125 °C. A sharp weight loss of HA-Gd_2O_3-PLNPs from 250 °C to 450 °C is attributed to the decomposition of the HA moieties, which accounts for 10% (wt%) of HA-Gd_2O_3-PLNPs (Fig. 3B and Fig. S10, ESI†).

As shown in Fig. 4A, the PLNP powder can be excited by a broad range of light with a large excitation peak at 268 nm due to the charge transfer of the zinc gallate host. The other three peaks at 407 nm, 463 nm and 558 nm are all ascribed to the d–d transitions of Cr from $^4A_2 \rightarrow {}^4T_1(te^2)$ transition, $^4A_2 \rightarrow {}^4T_1(t^2e)$ transition and $^4A_2 \rightarrow {}^4T_2(t^2e)$ transition, respectively. The $^4A_2 \rightarrow {}^4T_2(t^2e)$ transition is also the main reason for re-activation with a LED lamp irradiation (Fig. S11, ESI†).[22] The prepared PLNPs show excellent NIR PL with the peak at 695 nm originating from the $^2E \rightarrow {}^4A_2$ transition of Cr^{3+} (Fig. 4B).[41,42,44] The PL signal of the PLNPs can still be detected 2 h after stopping UV excitation (Fig. 4C and E) and re-activated with a LED lamp irradiation to recover the PL signal (Fig. 4D). The aqueous solution of PLNPs displays similar PL properties (Fig. 4F and G). The low density of PLNPs in aqueous solution is responsible for the weaker PL intensity than PLNP powder. HA-Gd_2O_3-PLNPs show similar excitation and emission spectra, but exhibit lower PL intensity than the PLNPs due to the lower density of PLNPs in the probe (Fig. S12, ESI†).

The cytotoxicity of the HA-Gd_2O_3-PLNPs was assessed with HepG 2 tumor cells and MCF-7 tumor cells. No distinct changes in the cell viability were observed after incubation with the HA-Gd_2O_3-PLNPs even with the concentration as high as 400 μg mL^{-1} for 24 h (Fig. S13, ESI†). The *in vitro* targeting capability of the HA-Gd_2O_3-PLNPs was evaluated with HepG 2 cells and MCF-7 cells. After 24 h incubation, a higher luminescence signal was observed in HepG 2 cells than those in both MCF-7 cells and HA-blocked HepG 2 cells (Fig. 5), indicating that HA-Gd_2O_3-PLNPs can specifically target CD44R on the surface of cancer cells.

The PL signal of the HA-Gd_2O_3-PLNPs in a normal nude mouse can be detected on a CCD camera for at least half an hour and recovered with a red LED light irradiation (Fig. 6A).

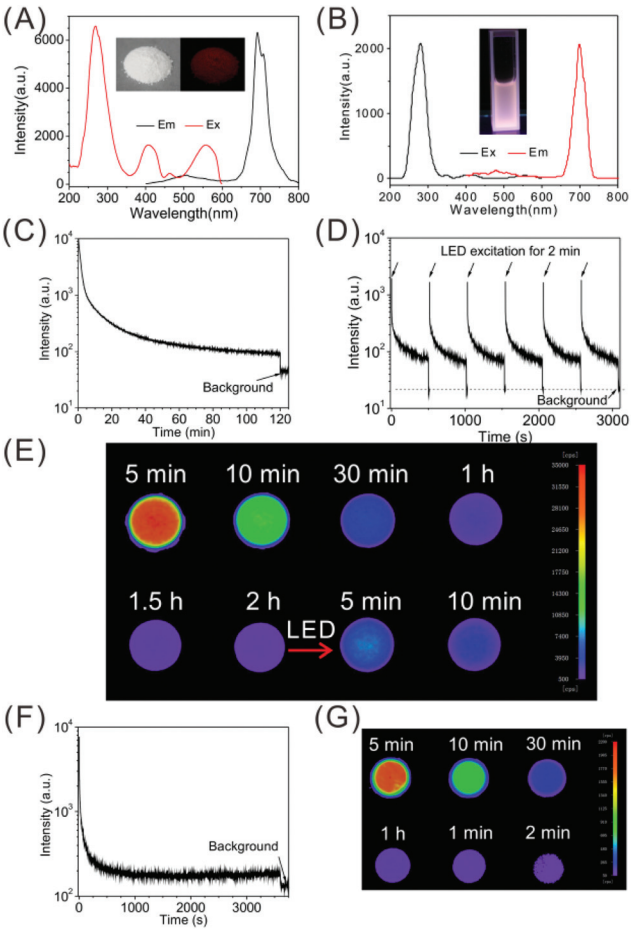

Fig. 4 (A) Excitation and emission spectra of the powder of the PLNPs. The inset represents the photoimages of the powder of the PLNPs in bright field (left) and after 5 min UV lamp excitation (right). (B) Excitation and emission spectra of the aqueous PLNP dispersion (2 mg mL^{-1}). The inset refers to the photoimage of the PLNP aqueous solution under the UV lamp excitation. (C) NIR PL delay curve of the PLNPs powder excited with a 254 nm UV lamp for 5 min. (D) NIR PL delay curve of the PLNP powder excited with red LED light repeatedly for 2 min. (E) NIR PL images of the PLNP powder after 5 min excitation with a 254 nm UV lamp and 2 min re-activation with red LED light. (F) NIR PL delay curve of the PLNP aqueous solution (2 mg mL^{-1}) excited with a 254 nm lamp for 5 min. (G) PL images of the PLNP aqueous solution after 10 min excitation with a 254 nm UV lamp and 2 min re-activation with red LED light. Exposure time: 10 s.

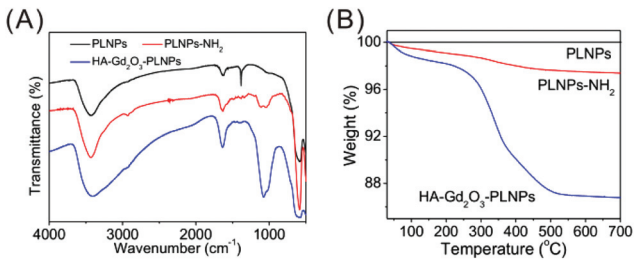

Fig. 3 (A) FT-IR spectra of the PLNPs, PLNPs-NH_2 and HA-Gd_2O_3-PLNPs. (B) TGA curves of the PLNPs, PLNPs-NH_2 and HA-Gd_2O_3-PLNPs.

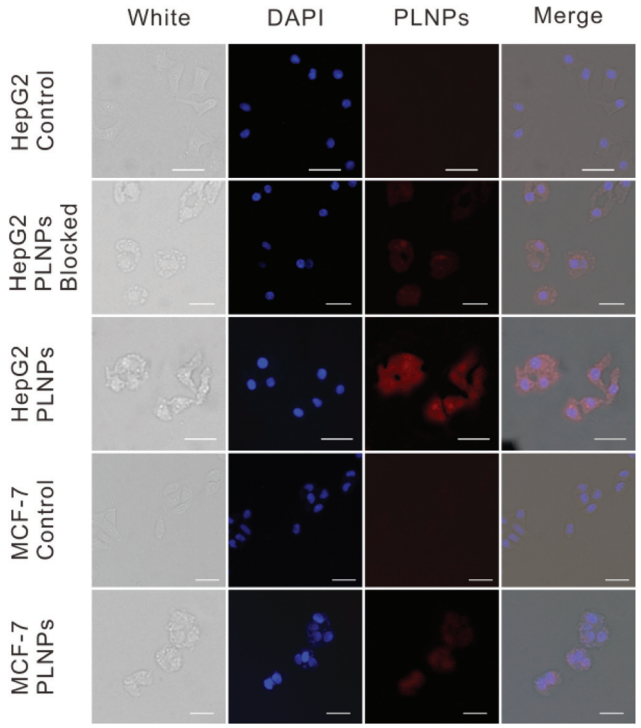

Fig. 5 Luminescence cell images of HepG 2 and MCF-7 tumor cells incubated with HA-Gd_2O_3-PLNPs for 24 h. All scale bars are 100 μm.

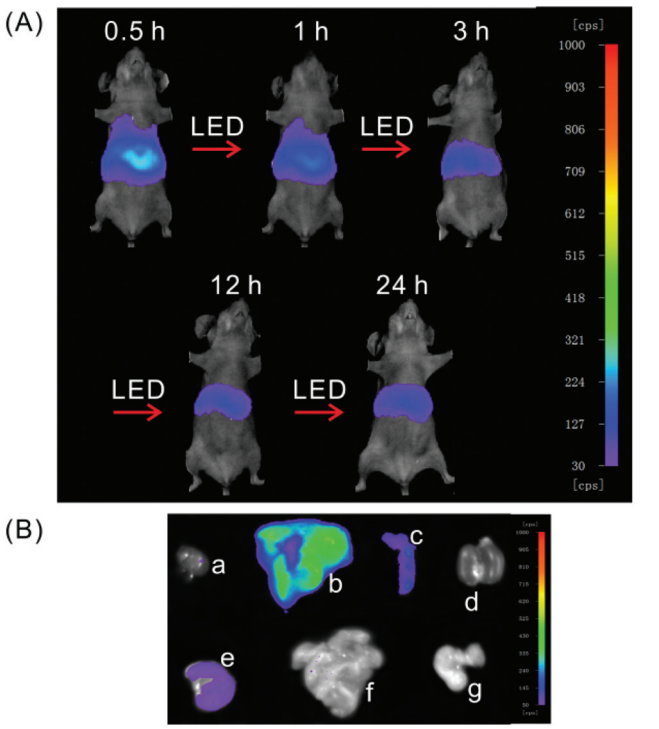

Fig. 6 (A) *In vivo* PL images of normal mice after intravenous injection of HA-Gd_2O_3-PLNPs (200 μL, 1 mg mL^{-1}). (B) Representative *ex vivo* PL images of isolated organs from a normal mouse at 24 h after tail vein injection of HA-Gd_2O_3-PLNPs (200 μL, 1 mg mL^{-1}): (a) heart, (b) liver, (c) spleen, (d) kidney, (e) lung, (f) intestine, (g) stomach.

No autofluorescence background signal was detected because of the *ex situ* excitation. The major PL signal was observed at the liver and spleen sites due to the rapid phagocytosis of the mononuclear phagocyte system and abundant capillary vessels in the lung might be the reason for the PL signal in the lung (Fig. 6B).[16,22] *In vivo* PL images of HA-Gd_2O_3-PLNPs in the tumor nude mice gave similar results except for the PL signal of the tumor sites (Fig. 7A). Three hours after the intravenous injection of HA-Gd_2O_3-PLNPs, the PL signal was observed in the tumor site and enhanced until 6 h post-injection. The *ex vivo* PL images of the tissues further demonstrate the tumor-targeting capability of HA-Gd_2O_3-PLNPs (Fig. 7B).

To evaluate the MRI capability of HA-Gd_2O_3-PLNPs, the longitudinal proton relaxation time (T_1) of a series of aqueous solutions of HA-Gd_2O_3-PLNPs with different Gd concentrations was measured to obtain the r_1 value. T_1-Weighted MR images of the HA-Gd_2O_3-PLNPs and Gd-DTPA reveal that the MR signal increased with the Gd concentration (Fig. 8A). The r_1 value of the HA-Gd_2O_3-PLNPs was 7.38 mM^{-1} s^{-1}, higher than that of Gd-DTPA (4.44 mM^{-1} s^{-1}) (Fig. 8B).

In vivo T_1-weighted MR images of nude mice were obtained to show the target capability of HA-Gd_2O_3-PLNPs (Fig. 8C). The MRI signal appeared in the liver and tumor sites 6 h after injection of HA-Gd_2O_3-PLNPs. The results were consistent with the PL images but with better spatial resolution. The above results demonstrate the potential of the HA-Gd_2O_3-PLNPs for T_1-weighted MRI.

The histological examination of the main organs from the nude mice, including heart, liver, spleen, kidney and lung, was

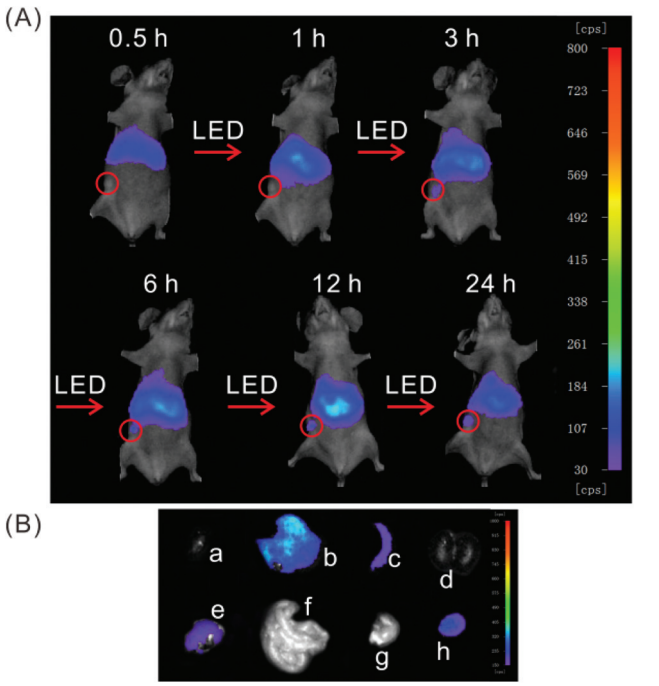

Fig. 7 (A) *In vivo* PL images of HepG 2 tumor balb/c nude mice after intravenous injection of 200 μL aqueous solution of HA-Gd_2O_3-PLNPs (1 mg mL^{-1}). (B) Representative *ex vivo* PL images of isolated organs from the tumor mouse at 24 h after tail vein injection of 200 μL aqueous solution of HA-Gd_2O_3-PLNPs (1 mg mL^{-1}): (a) heart, (b) liver, (c) spleen, (d) kidney, (e) lung, (f) intestine, (g) stomach, (h) tumor.

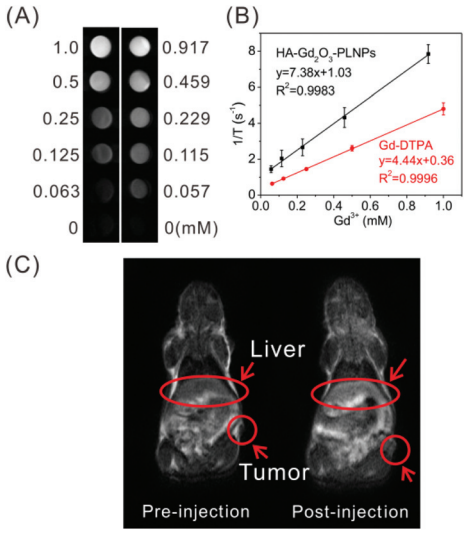

Fig. 8 (A) T_1-Weighted MR images of Gd-DTPA (left) and HA-Gd_2O_3-PLNPs (right) with various concentrations of Gd. (B) r_1 relaxivity curves of HA-Gd_2O_3-PLNPs and Gd-DTPA. (C) *In vivo* T_1-weighted MR images of the mouse treated with 200 μL aqueous solution of HA-Gd_2O_3-PLNPs (2 mg mL^{-1}) before and 6 h after the intravenous injection. The red cycles refer to the liver and tumor sites.

performed to evaluate the toxicity of HA-Gd_2O_3-PLNPs and no obvious pathological changes were observed (Fig. S14, ESI†). The body weight changes of the mice were monitored for 30 days after the intravenous injection of HA-Gd_2O_3-PLNPs, and the mice injected with PBS served as the control group. The body weight of two groups showed no distinct difference over 30 days (Fig. S15, ESI†). All results indicate no significant *in vivo* toxicity of HA-Gd_2O_3-PLNPs for biological application.

4. Conclusions

In conclusion, we have reported the design and fabrication of functional PLNP based multi-modal probe HA-Gd_2O_3-PLNPs for targeted PL/MR dual-modal bioimaging. The NIR emitting PLNPs with small particle size and uniform morphology have been directly synthesized by a hydrothermal method and conjugated to HA-Gd_2O_3 with good longitudinal relaxivity. The HA moieties of HA-Gd_2O_3 enable tumor-targeting capability of the probe. The conjugation of HA-Gd_2O_3 and PLNPs provides a convenient approach for the preparation of a targeted PL/MR multimodal probe with high PL signal-to-noise ratios and good MR spatial resolution.

Acknowledgements

The authors appreciate the support from the National Natural Science Foundation of China (21435001) and Open Funds of the State Key Laboratory of Electroanalytical Chemistry (SKLEAC201705).

Notes and references

1 Y.-F. Ma, J. Huang, S.-J. Song, H.-B. Chen and Z.-J. Zhang, *Small*, 2016, **12**, 4936–4954.
2 R. Weissleder and M. J. Pittet, *Nature*, 2008, **452**, 580–589.
3 Y.-Y. Wu, D.-Y. Gao, P.-F. Zhang, C.-S. Li, Q. Wan, C. Chen, P. Gong, G.-H. Gao, Z.-H. Sheng and L.-T. Cai, *Nanoscale*, 2016, **8**, 775–779.
4 T.-H. Shin, Y. Choi, S. Kim and J. Cheon, *Chem. Soc. Rev.*, 2015, **44**, 4501–4516.
5 Y.-D. Jin, *Acc. Chem. Res.*, 2014, **47**, 138–148.
6 H. F. Brito, J. Holsa, T. Laamanen, M. Lastusaari, M. Malkamaki and L. C. V. Rodrigues, *Opt. Mater. Express*, 2012, **2**, 371–381.
7 Y.-X. Zhuang, Y. Katayama, J. Ueda and S. Tanabe, *Opt. Mater.*, 2014, **36**, 1907–1912.
8 Y. Li, M. Gecevicius and J.-R. Qiu, *Chem. Soc. Rev.*, 2016, **45**, 2090–2136.
9 K. Van den Eeckhout, P. F. Smet and D. Poelman, *Materials*, 2010, **3**, 2536–2566.
10 K. Van den Eeckhout, D. Poelman and P. F. Smet, *Materials*, 2013, **6**, 2789–2818.
11 Q. le Masne de Chermont, C. Chanéac, J. Seguin, F. Pellé, S. Maîtrejean, J.-P. Jolivet, D. Gourier, M. Bessodes and D. Scherman, *Proc. Natl. Acad. Sci. U. S. A.*, 2007, **104**, 9266–9271.
12 T. Maldiney, A. Lecointre, B. Viana, A. Bessière, M. Bessodes, D. Gourier, C. Richard and D. Scherman, *J. Am. Chem. Soc.*, 2011, **133**, 11810–11815.
13 A. Abdukayum, J.-T. Chen, Q. Zhao and X.-P. Yan, *J. Am. Chem. Soc.*, 2013, **135**, 14125–14133.
14 F. Liu, W.-Z. Yan, Y.-J. Chuang, Z.-P. Zhen, J. Xie and Z.-W. Pan, *Sci. Rep.*, 2013, **3**, 1554.
15 A. Abdukayum, C.-X. Yang, Q. Zhao, J.-T. Chen, L.-X. Dong and X.-P. Yan, *Anal. Chem.*, 2014, **86**, 4096–4101.
16 Y.-C. Lu, C.-X. Yang and X.-P. Yan, *Nanoscale*, 2015, **7**, 17929–17937.
17 S.-Q. Wu, C.-W. Chi, C.-X. Yang and X.-P. Yan, *Anal. Chem.*, 2016, **88**, 4114–4121.
18 H.-X. Zhao, C.-X. Yang and X.-P. Yan, *Nanoscale*, 2016, **8**, 18987–18994.
19 Z.-J. Li, H.-W. Zhang, M. Sun, J.-S. Shen and H.-X. Fu, *J. Mater. Chem.*, 2012, **22**, 24713–24720.
20 Y.-J. Li and X.-P. Yan, *Nanoscale*, 2016, **8**, 14965–14970.
21 Z.-J. Li, Y.-W. Zhang, X. Wu, L. Huang, D.-S. Li, W. Fan and G. Han, *J. Am. Chem. Soc.*, 2015, **137**, 5304–5307.
22 T. Maldiney, A. Bessière, J. Seguin, E. Teston, S. K. Sharma, B. Viana, A. J. J. Bos, P. Dorenbos, M. Bessodes, D. Gourier, D. Scherman and C. Richard, *Nat. Mater.*, 2014, **13**, 418–426.
23 E. Teston, S. Richard, T. Maldiney, N. Lièvre, G. Y.-S. Wang, L. Motte, C. Richard and Y. Lalatonne, *Chem. – Eur. J.*, 2015, **21**, 7350–7354.
24 B.-Y. Wu, H.-F. Wang, J.-T. Chen and X.-P. Yan, *J. Am. Chem. Soc.*, 2011, **133**, 686–688.

25 Y.-R. Tang, H.-J. Song, Y.-Y. Su and Y. Lv, *Anal. Chem.*, 2013, **85**, 11876–11884.
26 N. Li, W. Diao, Y.-Y. Han, W. Pan, T.-T. Zhang and B. Tang, *Chem. – Eur. J.*, 2014, **20**, 16488–16491.
27 N. Li, Y.-H. Li, Y.-Y. Han, W. Pan, T.-T. Zhang and B. Tang, *Anal. Chem.*, 2014, **86**, 3924–3930.
28 B.-Y. Wu and X.-P. Yan, *Chem. Commun.*, 2015, **51**, 3903–3906.
29 Z.-J. Li, Y.-J. Zhang, H.-W. Zhang and H.-X. Fu, *Microporous Mesoporous Mater.*, 2013, **176**, 48–54.
30 T. Maldiney, B. Ballet, M. Bessodes, D. Scherman and C. Richard, *Nanoscale*, 2014, **6**, 13970–13976.
31 J.-P. Shi, X. Sun, J.-L. Li, H.-Z. Man, J.-S. Shen, Y.-K. Yu and H.-W. Zhang, *Biomaterials*, 2015, **37**, 260–270.
32 J.-P. Shi, H.-X. Fu, X. Sun, J.-S. Shen and H.-W. Zhang, *J. Mater. Chem. B*, 2015, **3**, 635–641.
33 W.-B. Dai, Y.-F. Lei, S. Ye, E.-H. Song, Z. Chen and Q.-Y. Zhang, *J. Mater. Chem. B*, 2016, **4**, 1842–1852.
34 R. Abdurahman, C.-X. Yang and X.-P. Yan, *Chem. Commun.*, 2016, **52**, 13303–13306.
35 L.-J. Chen, S.-K. Sun, Y. Wang, C.-X. Yang, S.-Q. Wu and X.-P. Yan, *ACS Appl. Mater. Interfaces*, 2016, **8**, 32667–32674.
36 S.-Q. Wu, C.-X. Yang and X.-P. Yan, *Adv. Funct. Mater.*, 2017, **27**, 1604992.
37 B. B. Srivastava, A. Kuang and Y.-B. Mao, *Chem. Commun.*, 2015, **51**, 7372–7375.
38 T. Maldiney, B.-T. Doan, D. Alloyeau, M. Bessodes, D. Scherman and C. Richard, *Adv. Funct. Mater.*, 2015, **25**, 331–338.
39 E. Teston, Y. Lalatonne, D. Elgrabli, G. Autret, L. Motte, F. Gazeau, D. Scherman, O. Clement, C. Richard and T. Maldiney, *Small*, 2015, **11**, 2696–2704.
40 H.-Y. Wang, Y.-Y. Fu, X.-J. Zhang, C.-S. Yu and S.-K. Sun, *RSC Adv.*, 2015, **5**, 93041–93047.
41 Z.-W. Pan, Y.-Y. Lu and F. Liu, *Nat. Mater.*, 2012, **11**, 58–63.
42 A. Bessière, S. Jacquart, K. Priolkar, A. Lecointre, B. Viana and D. Gourier, *Opt. Express*, 2011, **19**, 10131–10137.
43 P. Coimbra, P. Alves, T. A. M. Valente, R. Santos, I. J. Correia and P. Ferreira, *Int. J. Biol. Macromol.*, 2011, **49**, 573–579.
44 A. Bessière, S. K. Sharma, N. Basavaraju, K. R. Priolkar, L. Binet, B. Viana, A. J. J. Bos, T. Maldiney, C. Richard, D. Scherman and D. Gourier, *Chem. Mater.*, 2014, **26**, 1365–1373.